

Optical and acoustic plasmons in the layered material Sr_2RuO_4

J. Schultz,^{1,*} A. Lubk,^{1,2} F. Jerzembeck,³ N. Kikugawa,⁴ M. Knupfer,¹ D. Wolf,¹ B. Büchner,^{1,2} and J. Fink^{1,2,†}

¹*Leibniz Institute for Solid State and Materials Research Dresden, Helmholtzstraße 20, 01069 Dresden, Germany*

²*TU Dresden, Institute of Solid State and Materials Physics, Haeckelstraße 3, 01069 Dresden, Germany*

³*Max Planck Institute for Chemical Physics of Solids,
Nöthnitzer Straße 40, D-01187 Dresden, Germany*

⁴*National Institute for Materials Science, Tsukuba 305-0003, Japan*

(Dated: July 8, 2024)

I. ABSTRACT

We use momentum-dependent electron energy-loss spectroscopy in transmission to study collective charge excitations in the layer metal Sr_2RuO_4 . This metal has a transition from a perfect Fermi liquid below $T \approx 30$ K into a "strange" metal phase above $T \approx 800$ K. We cover a complete range between in-phase and out-of-phase oscillations. Outside the classical range of electron-hole excitations, leading to a Landau damping, we observe well-defined plasmons. The optical (acoustic) plasmon due to an in-phase (out-of-phase) charge oscillation of neighbouring layers exhibits a quadratic (linear) positive dispersion. Using a model for the Coulomb interaction of the charges in a layered system, it is possible to describe the range of optical plasmon excitations at high energies in a mean-field random phase approximation without taking correlation effects into account. In contrast, RIXS data show at low energies an enhancement of the acoustic plasmon velocity due to correlation effects. This difference can be explained by an energy dependent effective mass which changes from ≈ 4 at low energy to 1 at high energy near the optical plasmon energy. There are no signs of over-damped plasmons predicted by holographic theories.

II. PLASMONS IN "STRANGE" METALS

"Strange" metals are at present one of the most interesting research fields in solid state physics [1]. Due to the strong interaction between their charge carriers, they show a deviation from the Fermi-liquid behaviour, e.g., they do not show a quadratic but a linear temperature dependence of the electrical resistivity or linear in energy scattering rate in Angle-Resolved Photoemission Spectroscopy (ARPES) [2, 3]. Moreover, there is no saturation at the Mott-Ioffe-Regel limit [4]. The unconventional and in some cases high-temperature superconduc-

tivity detected in these materials is supposed to be related to their "strange" normal-state electronic structure. Doped cuprates are prototypes of these "strange" metals. The non-Fermi liquid properties could be explained by a continuum of excitations up to an ultraviolet cutoff frequency ω_c in the electronic susceptibility [5], leading to a phenomenological marginal Fermi liquid theory. Integrating over this continuum yields a linear in energy imaginary part of the self-energy or scattering rate [6]. Electron Energy-Loss Spectroscopy (EELS) is a suitable experimental method to verify the existence of such a continuum because it measures the imaginary part of the electronic susceptibility $\Im[\chi(\mathbf{q}, \omega)]$. Here \mathbf{q} is the momentum and ω is the energy. In nearly-free electron metals, there exists a $2k_F$ wide stripe of a continuum of particle-hole excitations [7] which starts at $q_{\text{crit}} \approx \omega/v_F$, where v_F is the Fermi velocity. In simple metals collective excitations (plasmons) exist at the order of the Fermi energy. At higher energies they are (Landau) damped by a decay into particle-hole excitations above the critical momentum: $q_{\text{crit}} \approx \omega_P/v_F$. Usually, q_{crit} is between half and one \AA^{-1} .

Surprisingly, early transmission EELS (T-EELS) studies of the highly correlated doped cuprates, using dedicated T-EELS spectrometers [8–10] with high momentum resolution, showed this behavior with a weak damping of plasmons below q_{crit} [11–16]. On the other hand, T-EELS studies using transmission electron microscopes with weak momentum resolution [17, 18] showed no plasmon at 0.3 \AA^{-1} but a continuum. The difference can be easily explained by the poor momentum resolution in the TEM experiments ($\Delta q = 10$ and 30 \AA^{-1}) which averages over the whole Brillouin zone (BZ) and therefore measures predominantly the Landau continuum above q_{crit} .

At variance with the early T-EELS measurements of collective excitations in hole doped cuprates great attention attracted the prediction of over-damped plasmons in "strange" metals and a replacement of these excitations by a continuum [19]. The authors concluded that a new kind of theory of strongly interacting matter may be needed to explain this. The latter may also be connected to the phenomenon of high- T_c superconductivity. The over-damped plasmon was discussed in terms of holographic theories, which predicted, different from the classical Landau damping, a strong damping even for the long wavelength plasmons due to quantum critical fluctuations. Recently, this work was supported by similar

* j.schultz@ifw-dresden.de

† j.fink@ifw-dresden.de

calculations [20].

Furthermore, there are several recent experimental EELS experiments in reflection (R-EELS), supporting the theories which predict over-damped plasmons in "strange" or highly correlated metals. Only at very small momenta a well-defined plasmon exists followed by a transition into a featureless momentum-independent constant-in-frequency continuum well below q_{crit} [21–24]. Moreover, there is a very recent ARPES study on doped cuprates in which these holographic theories are supported by an asymmetric line shape at higher energies [25].

There are other differences between T- and R-EELS results from hole-doped cuprates: At small q , i.e. long wave length, T-EELS data show a positive dispersion which can be explained in RPA using an unrenormalised band structure [11, 12, 14, 26]. On the other hand, R-EELS data show a negative dispersion, which may indicate a more localised electron liquid. The hybridisation of the d-bands with the s-band in the alkali metals or many-body effects, when moving from Na to Cs is supposed to turn the plasmon dispersion from positive to negative [27, 28]. On the other hand, the different result between T-EELS and R-EELS possibly can be explained by different response functions with respect to surface and bulk properties.

In this context, we mention that in various cuprates, well pronounced dispersive acoustic plasmons were detected by RIXS [29–31]. In all these measurements, weakly damped plasmons were detected for momentum ranging up to half of the size of the BZ.

For understanding the differences between T- and R-EELS on cuprates and to understand the influence of correlation effects on collective charge oscillation in general, we present here T-EELS data on the related metal Sr_2RuO_4 [32, 33]. It is in some way intermediate between a normal Fermi liquid metal and a strange metal. Below ≈ 30 K it is a perfect Fermi liquid which transforms at low temperatures $T_c = 1.5$ K into an unconventional superconductor [34]. It has other similarities to the cuprates: it has a perovskite structure formed by transition metal oxides layers. The essentially 2D correlated electronic structure is formed by three bands and has a van Hove singularity close to the Fermi level.

Deviating from the cuprate high T_c superconductors, it is a stoichiometric compound without crystallographic disorder due to dopant ions. Furthermore, the temperature dependence of the transport properties are more complicated. Above $T \approx 30$ K there is a crossover region in which Sr_2RuO_4 exceeds at $T_{\text{MIR}} \approx 800$ K the Mott-Ioffe-Regel limit, i.e., it turns to a "bad metal". These transport properties are partially related to Hund's rule coupling which causes strong correlation effects far from the insulating state [35].

Recently, we have studied the electronic structure of Sr_2RuO_4 by an investigation of the optical plasmon excitations with momenta parallel to the layers [36] using a dedicated T-EELS spectrometer [10]. Also in this highly

correlated material, a well-defined plasmon could be detected near 1.5 eV. The plasmon has a *positive* dispersion and decays into a continuum of particle-hole excitations due to Landau damping, which could be explained in the framework of the random phase approximation (RPA) using an *unrenormalised* band structure.

Most of the previous momentum dependent EELS studies on layered materials were performed for a wave vector parallel to the layers. The reason for this is that thin samples (T-EELS) or clean surfaces (R-EELS) are easily prepared by a cleavage of the crystals parallel to the layers. In the present work, by focused ion beam milling, we are able to prepare thin electron transparent lamella in which the layers are perpendicular to the surface. Using such samples, it was for the first time possible to map out a complete set of plasmon excitations with momentum between parallel and perpendicular to the layers almost in the entire BZ. In this way, it is possible to control theoretical work on plasmon excitations in layered compounds, which is available since many decades [37–40].

At present, there is a strong discussion, whether spectroscopic results on the damping and dispersion of plasmons can be explained on the basis of mean field theories such as RPA or whether we need new theories to explain valence band EELS results (see also the recent EELS review [41] which contrast the conflicting results of T-EELS and R-EELS). The present article strongly supports the results derived from T-EELS.

III. PLASMON DISPERSION IN LAYERED SYSTEMS

The dynamic structure factor is determined by the Fourier transformation of the charge density-density correlation function. It can be expressed [42] by the dynamical susceptibility $\chi(\mathbf{q}, \omega)$:

$$S(\mathbf{q}, \omega) \propto \Im[\chi(\mathbf{q}, \omega)] \propto \Im\left[-\frac{1}{\epsilon(\mathbf{q}, \omega)}\right]. \quad (1)$$

Here, $\epsilon(\mathbf{q}, \omega)$ is the complex dielectric function.

The calculation of the susceptibility of the many-body system of the charge carriers in solids is a challenging task. The susceptibility χ_0 for a non-interacting one-band electron liquid is given by [43]:

$$\chi_0(\omega, \mathbf{q}) = \int_{\text{BZ}} A(\mathbf{q}, \mathbf{k}) \frac{2F(\mathbf{k})\Delta E(\mathbf{q}, \mathbf{k})}{(\omega + i\Gamma)^2 - \Delta E^2(\mathbf{q}, \mathbf{k})} d^3k. \quad (2)$$

Here $\Delta E = E_{\mathbf{k}+\mathbf{q}} - E_{\mathbf{k}}$, $E_{\mathbf{k}}$ are the band energies of the electrons having a momentum \mathbf{k} , $A(\mathbf{q}, \mathbf{k})$ is related to matrix elements, Γ is the lifetime broadening of the particle-hole excitations, and $F(\mathbf{k})$ is the Fermi function.

While χ_0 is the Lindhard susceptibility for single-particle excitations related to an external field, stemming from the field of the scattering electron, χ is the susceptibility for the total field, including the induced one. Running a self-consistency cycle, we obtain the mean field

RPA result:

$$\chi^{\text{RPA}}(\mathbf{q}, \omega) = \frac{\chi_0(\mathbf{q}, \omega)}{\epsilon_b - V(\mathbf{q})\chi_0(\mathbf{q}, \omega)}. \quad (3)$$

Here, $V(\mathbf{q})$ is the Fourier transformed Coulomb interaction between the charge carriers and ϵ_b is the background dielectric constant.

In this approximation and for small damping, there are in addition to the single-particle excitations collective excitations, termed plasmons. The energy of the plasmon is determined by the zeros of the real part of the denominator of Eq. (3). The long wavelength energy of the plasmon in the RPA is given by

$$\omega_P(0)^2 = \frac{4\pi N e^2}{\epsilon_b m^*} \quad (4)$$

with N being the density of the charge carriers, m^* the effective mass, and e the elementary charge.

For small but finite momentum, up to q^2 and within the RPA, the dispersion is given by

$$\omega_P(q) = \omega_P(0) + A_{\text{RPA}} q^2 + \dots; \quad A_{\text{RPA}} = \frac{\hbar}{m}(\alpha_1 + \alpha_2). \quad (5)$$

α_1 is determined by the finite compressibility of the electron liquid and is always positive. α_2 , which is always negative, is proportional to the size of the effective mass [26]. For free-electron metals only

$$\alpha_1 = \frac{m}{\hbar\omega_P(0)} \frac{3}{10} \langle v_{\text{F}}^2 \rangle_{\mathbf{q}} \quad (6)$$

determines the optical plasmon dispersion. Here, the averaged squared Fermi velocity along the \mathbf{q} direction is defined by [14]

$$\langle v_{\text{F}}^2 \rangle_{\mathbf{q}} = \left\langle \left(\frac{\mathbf{q}}{\hbar q} \frac{\partial E_{\mathbf{k}}}{\partial \mathbf{k}} \right)^2 \right\rangle. \quad (7)$$

For metals where the band dispersion is strongly reduced by a finite effective mass m^* , the negative α_2 may dominate the optical plasmon dispersion, leading in total to a negative dispersion [26].

When the plasmon merges into the single-particle continuum, it decays into particle-hole excitations. This process is termed Landau damping.

In the following we discuss the structure factor $V(\mathbf{q})$. In a homogeneous electron system

$$V(\mathbf{q}) = \frac{4\pi e^2}{q^2}. \quad (8)$$

For a system, built up by 2D layers separated by the distance d we use the Fetter model with the Coulomb potential

$$V(\mathbf{q}) = V(q_{\parallel}, q_{\perp}) = \frac{4\pi e^2}{q^2} \frac{q_{\parallel} d}{2} \frac{\sinh(q_{\parallel} d)}{\cosh(q_{\parallel} d) - \cos(q_{\perp} d)}, \quad (9)$$

where q_{\parallel} (q_{\perp}) is the momentum parallel (perpendicular) to the layer [38]. Therefore, in a layered system, the plasmon dispersion is not only determined by the compressibility of the electron liquid (see Eq. 5) but also by the structure factor $V(\mathbf{q})$:

$$\omega_P(q)^2 = s^2 q_{\parallel}^2 + \omega_P(0)^2 \frac{q_{\parallel} d}{2} \frac{\sinh(q_{\parallel} d)}{\cosh(q_{\parallel} d) - \cos(q_{\perp} d)} \quad (10)$$

with $s^2 = \frac{1}{2} \langle v_{\text{F}}^2 \rangle_{\mathbf{q}}$. For a dielectric function that is consistent with the above dispersion relation we refer to the Method section. For small q_{\parallel} and $q_{\perp} d = 0$, the structure factor $V(q_{\parallel}, q_{\perp})$ is the same as in the homogeneous electron gas. In this case, the charge oscillations in the layers are in phase and the plasmon dispersion is the same as in a homogeneous 3D electron system. For $q_{\perp} d = \pi$ the charge oscillations between neighboring layers are out of phase.

This leads to an acoustic plasmon, with a rather small energy gap due to the layer interaction [44] in the long wave length limit. The dispersion of the acoustic plasmon for small q_{\parallel} is given by

$$\omega_P(q_{\parallel}) = q_{\parallel} \sqrt{s^2 + \omega_P(0)^2 \frac{d^2}{4}}. \quad (11)$$

Very often, the first term in the square root is considerably smaller than the second. Then the phase velocity of the acoustic plasmon along the direction of q_{\parallel} is given by

$$v_p = \frac{\omega_P(0)d}{2}. \quad (12)$$

Besides the hydrodynamic Fetter model, the plasmon dispersion of a layered system was also derived by means of RPA, leading to similar results [45].

IV. EELS DATA

T-EELS measurements were performed on single-crystalline Sr_2RuO_4 layers at room temperature. Fig. 1 shows the crystal structure of Sr_2RuO_4 which consists of RuO_2 layers stacked with SrO spacer layers along the \mathbf{c} -axis direction. The thin films were characterized by *in-situ* electron diffraction and the crystallographic axes were oriented with respect to the (\mathbf{a}, \mathbf{c}) plane [see Fig. 2 (a)]. The distance $d = 6.36 \text{ \AA}$ between the RuO_2 layers is half the \mathbf{c} -axis lattice constant. The thin lamellas for T-EELS with a normal direction parallel to the \mathbf{b} -axis were cut with a focused ion beam. In this way, EELS experiments were possible with the momentum parallel to the (\mathbf{a}, \mathbf{c}) plane. We emphasize that this momentum range is different from our previous EELS study on Sr_2RuO_4 [36] where we covered the momentum range in the (\mathbf{a}, \mathbf{b}) plane.

T-EELS was performed with a primary electron energy of 80 keV and with an energy and momentum resolution

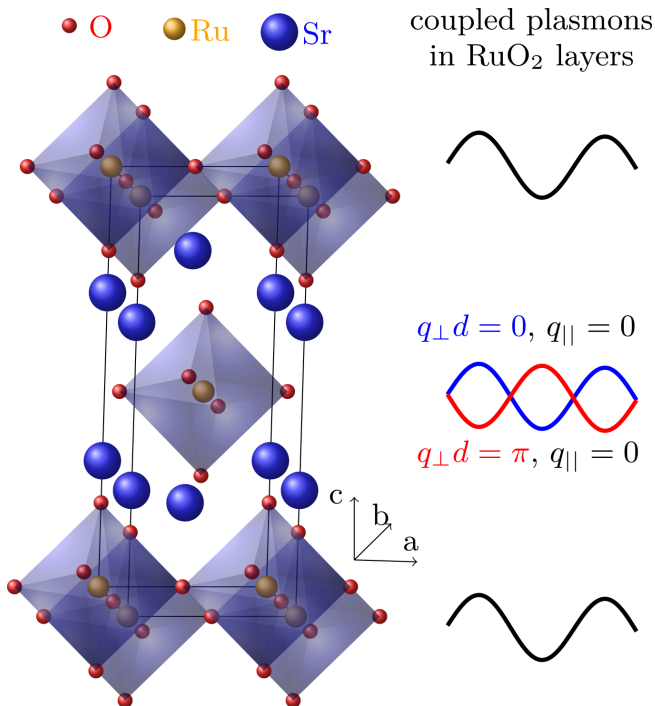


FIG. 1. Crystal structure of Sr₂RuO₄ and schematic representation of in-phase and out-of-phase two dimensional charge oscillations

of 120 meV and 0.04 \AA^{-1} , respectively. The momentum-resolved EELS data were sequentially recorded in the ($q_{\parallel} = q_a, q_{\perp}$) momentum plane as depicted in Fig. 2(b). In Fig. 3 we show typical EELS intensities as a function of the energy for various q_{\parallel} and q_{\perp} values. With increasing q_{\parallel} the plasmon energy slightly increases, whereas for increasing q_{\perp} the plasmon energies decrease. At low total momentum it is difficult to see a well defined plasmon due to the high intensity of the quasi-elastic peak. The same holds for high total momentum because the T-EELS cross section is decreasing with $1/q^2$ (see below). Except for the described cases, well developed and dispersing plasmon excitations below 1.8 eV are visible. From the fit to the data we obtain the energy, the width, and the intensity of the plasmon excitations (see Methods).

The energy is plotted in Fig. 4 as a function of q_{\parallel} for various q_{\perp} values together with theoretical curves calculated in the framework of the Fetter model (see Section III). We use the parameters $\omega_p(0) = 1.48 \text{ eV}$ (from optical spectroscopy [46]), $d = 6.36 \text{ \AA}$, and $\langle v_F^2 \rangle_{100} = 4.91 \text{ (eV \AA)}^2$. The latter value for the three Ru 4d t_{2g} bands crossing the Fermi level was derived from a tight-binding (TB) band structure [47] (see Methods). For all plasmon energies above the continuum, within error bars, there is rather good agreement between theory and experiment. There is a continuous transition between the optical plasmon for $q_{\perp} = 0$ (purple data) at higher energy to the acoustic plasmon ($q_{\perp} = 0.4 \text{ \AA}^{-1}$) close to $q_{\perp} = \pi/d = 0.49 \text{ \AA}^{-1}$ (red data) at lower energy. Due to our finite energy resolution we cannot follow the acoustic

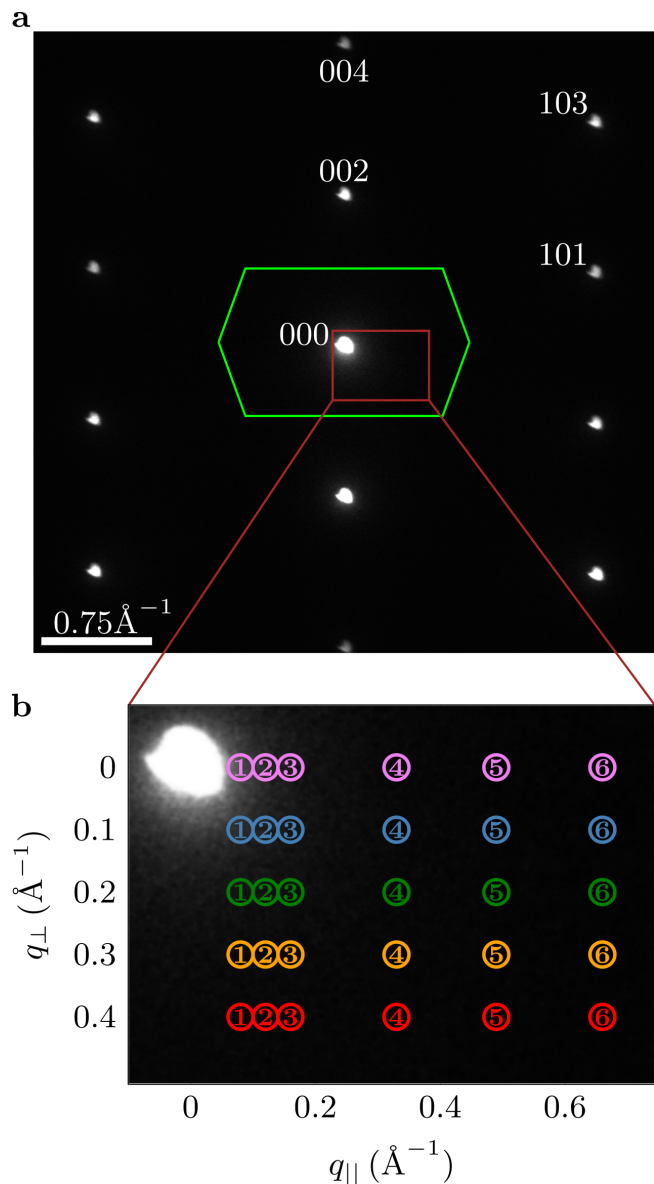


FIG. 2. (a) Indexed electron diffraction pattern (white dots) in the (q_{\parallel}, q_{\perp}) plane, including the reduced Brillouin zone (green) for equal layers along the c-axis. (b) Brown momentum range [see (a)] in which loss spectra are recorded for various q_{\parallel} and q_{\perp} values. The colours purple, blue, green, yellow, and red correspond to q_{\perp} equal 0, 0.1, 0.2, 0.3, and 0.4 \AA^{-1} , respectively. The diameter of the filter entrance aperture [indicated by the colored circles in (b)] defining the momentum range in one EEL spectrum (momentum resolution) corresponds to a momentum of 0.04 \AA^{-1} .

plasmon to zero energy. Furthermore the momentum resolution of the instrument is limited by the finite width of the collection aperture of our spectrometer. Since the signal is integrated over the latter we observe a drop of the plasmon energy also for the optical plasmon near $q_{\perp} = 0$ (see purple data in Fig. 4).

The difference between RPA dispersion and experimental data for $q_{\parallel} \geq q_{\text{crit}}$ can be explained by Landau

damping. For these wave vectors, the plasmon decays into the particle-hole excitations and the spectral weight is caused by the Lindhard continuum. This leads to a reduction of the energy of the maximum in the loss function. This reduction has been observed in our calculations presented in Ref. [36]. A similar behavior has been also observed for Al [48]. In Fig. 4 we also show the continuum of the single-particle intra-band transitions χ_0 (see the grey region) calculated using an unrenormalized TB band structure [47] (see Methods). The optical plasmon merges into the continuum near $q_{\parallel} \approx 0.4 \text{ \AA}^{-1}$. We assign this value to the critical momentum q_{crit} . This value is further corroborated by the rapid increase of the plasmon width at this wave vector (Fig. 5).

V. OPTICAL AND ACOUSTIC PLASMONS IN LAYERED "STRANGE" METALS

The data presented in Fig. 3 demonstrate that T-EELS in layered systems is capable of probing not only in-phase (optical) plasmons with momentum parallel to the layers but also out-of phase (acoustic) collective charge oscillations in neighboring layers. A suitable sample preparation is important for such studies. Thus, we show that T-EELS can compete with recent RIXS studies of acoustic plasmons of cuprates [29, 30, 44]. This is an important extension of T-EEL spectroscopy. Furthermore, we emphasize that the present work shows that acoustic plasmons exist also in non-cuprate "strange" metal layer systems.

Well defined plasmon exist in the complete range which is not covered by the range of single-particle excitations calculated in the mean-field RPA theory. Optical plasmons exist in $\approx 15 \%$ of the BZ. The rest is determined by a continuum of intra-band single particle excitations, which strongly dampen the plasmon excitation in excellent agreement with previous studies [36] (see Fig. 5). There is no sign of a reduction of the coherent plasmon range due to an over-damping discussed in terms of holographic theories [19, 20].

In the following we compare the present EELS results with theoretical predictions in a more quantitative way. In our previous publication we analyzed the plasmon dispersion by a calculation of the susceptibility together with an adjustment of the strength of the Coulomb potential to $\omega_{\text{P}}(0)$. The comparison with the experimental dispersion yields good agreement when using an unrenormalized TB band structure ($\frac{m^*}{m_0} = 1$) instead of a renormalized band structure with an effective mass $\frac{m^*}{m_0} \approx 4.5$ taken from angle-resolved photoemission spectroscopy (ARPES) experiments [49]. In this quite indirect analysis, we concluded that the plasmon dispersion is not influenced by the mass renormalization observed by ARPES.

Here we perform a similar, but much more direct analysis. Fitting the dispersion of the optical plasmon dispersion for $q \leq q_{\text{crit}} \approx 0.4 \text{ \AA}^{-1}$ (see Fig. 4 purple data) with

Eq. (1) we derive a dispersion coefficient $A = 1.8 \pm 0.8 (\text{eV\AA})^2$ which is in agreement with the more precise result from our previous publication $A = 2.1 \pm 0.2 (\text{eV\AA})^2$. Using the unrenormalized tight binding band structure [47] we receive a squared Fermi velocity $\langle v_{\text{F}}^2 \rangle_{100} = 3.4 (\text{eV\AA})^2$ and the dispersion coefficient $A = 2.5 (\text{eV\AA})^2$. The latter value is close to the experimental value. On the other hand, using the effective mass $\frac{m^*}{m_0} \approx 4.5$ from ARPES [49] we derive a negative dispersion with $A = -0.012 (\text{eV\AA})^2$ which is at variance with the experimental data. This effective mass dependence of the plasmon dispersion was already discussed in our previous paper [36]. Thus our present and the previous experimental data of the dispersion of the optical plasmon indicates that the long wavelength dispersion can be explained in the framework of a mean-field RPA theory.

In Fig. 5 we present the plasmon width as a function of q_{\parallel} . We show data derived from Fig. 3 and from our previous EELS experiments [36]. Within error bars there is a good agreement between the two datasets. The plasmon width at zero momentum is smaller than the plasmon energy, indicating a coherent collective charge excitation. The width below $q_{\parallel} = 0.3 \text{ \AA}^{-1}$ is constant. Near $q_{\parallel} = 0.4 \text{ \AA}^{-1}$ the width increases, indicating the merging of the plasmon dispersion into the single particle continuum at a $q_{\text{crit}} \approx 0.4 \text{ \AA}^{-1}$. (See also Fig. 4). As the calculations for the continuum are performed without band-renormalisation this indicates again that at the relative high plasmon energy, the effective mass is close to one and supports the formation of resilient quasi-particles [46].

In Fig. 6 we depict the plasmon intensities as a function of q_{\parallel} and q_{\perp} (see Methods section for details of the evaluation). The decay of the total spectral weight of the plasmon resonances at large momentum transfers is approximately proportional to q^{-2} as observed for conventional bulk plasmons and predicted by the longitudinal f-sum rule and the theoretical dielectric function of the Fetter model (see Methods). The decay observed for $q_{\perp} \neq 0$ in the long wavelength limit is also consistent with the theoretical dielectric response as well as a version of the long-wavelength sum rule implying that the full spectral weight at $q = 0$ is concentrated in the bulk plasmon $q_{\perp} = 0$ mode (see Methods and Ref. [50] for the sum rules). The shift of the maximal integrated loss intensity towards smaller momentum transfer predicted by theory may be attributed to shortcomings of the Fetter model dielectric function (see Methods), impact of the zero loss, and limited experimental resolution.

In the following we discuss the acoustic plasmon data (see red data and line in Fig. 4). Despite the gap at low energy due to a finite energy resolution, the dispersion extrapolates to zero energy typical of an acoustic plasmon. The derived experimental plasmon velocity is $v_{\text{P}} \approx 4.7 \text{ eV\AA}$. From Eq. (11) we derive $v_{\text{P}} \approx 4.8 \text{ eV\AA}$ in very good agreement with the experimental value. This indicates that the first term in Eq. (11) due to the finite Fermi velocity is small compared to the term which only depends on $\omega_{\text{P}}(0)$ and d . Thus, for a given $\omega_{\text{P}}(0)$ the

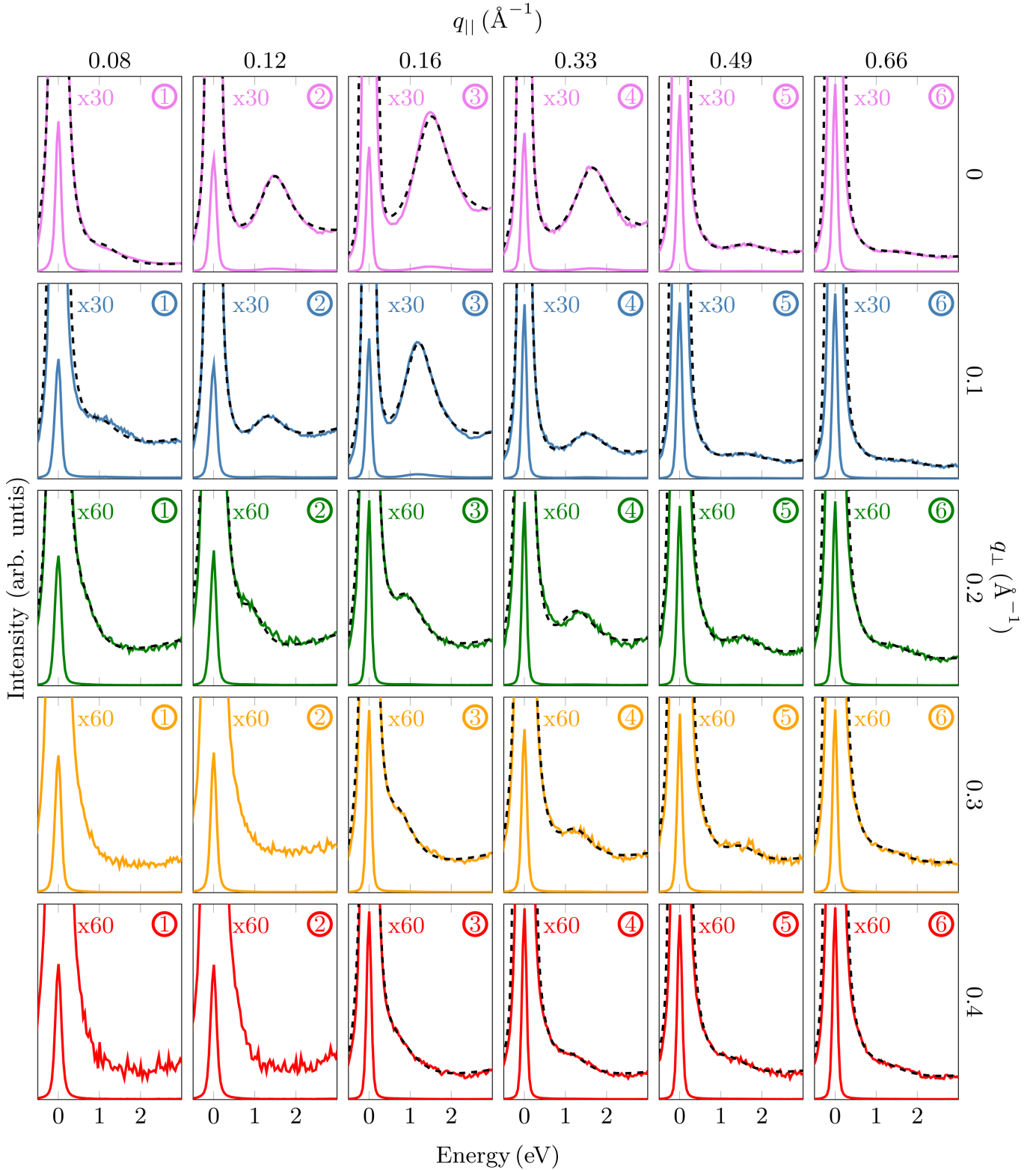


FIG. 3. Electron energy-loss intensities for various $q_{||}$ and q_{\perp} values. The indicated numbers (1-6) and the colors correspond to the momentum values depicted in Fig. 2. Experimental spectra are depicted twice (normal scale + 30x/60x scaled up) to show both the zero loss peak and the plasmon peak. The black dashed lines correspond to fits of a superposition of a Voigt profile (zero loss), a Drude function (plasmons), and a background (see Methods).

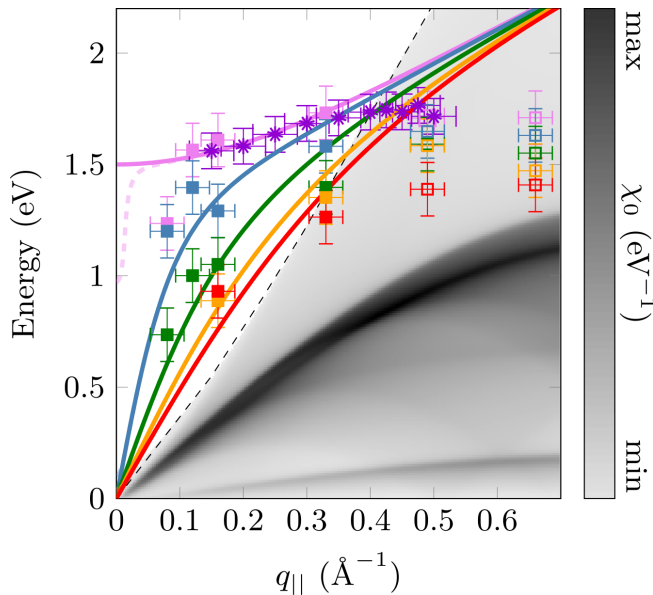


FIG. 4. Plasmon dispersion along the momentum q_{\parallel} parallel to the layers for several q_{\perp} perpendicular to the layers (squares) together with calculations within the framework of the Fetter model (solid lines). The q_{\perp} values 0, 0.1, 0.2, 0.3, and 0.4 \AA^{-1} are marked by purple, blue, green, yellow, and red colour symbols, respectively (see Fig. 3). We have added also the data from the optical plasmon dispersion derived in our previous publication (dark purple stars) [36]. The horizontal error bars originate from the finite momentum resolution while the vertical ones are related to the finite spectral resolution of the EEL spectrometer (the fitting error is small in comparison). The region marked in grey corresponds to the susceptibility χ_0 calculated from a tight binding band structure (see Methods). The excitations in the continuum range are marked by open symbols. The colored dashed curves represent theoretical curves considering finite momentum resolution, i.e., integration within the EEL collection aperture.

acoustic plasmon dispersion only depends on d and is not influenced by a large Fermi velocity but hints to a reduced one due to correlation effects (enhanced effective mass). Unfortunately, the finite energy resolution in the present T-EELS experiment does not allow a quantitative determination of the effective mass at low energies. However, RIXS data on cuprates indicate, that an enhanced effective mass is necessary to describe the plasmon velocity of the acoustic plasmons.

Neglecting the Fermi velocity term, the linear acoustic plasmon dispersion [see Eq. (11)] can be explained in the following way. The phase difference π of the oscillations between neighboring layers reduces the plasmon energy from $\omega_p(0)$ to zero. When adding a momentum q_{\parallel} the phase difference between neighboring layers is increased to $\pi + q_{\parallel}d$ and therefore, using a linear relation, the energy of the acoustic plasmon should increase by $(\omega_p(0)dq_{\parallel})/\pi$ which is close to Eq. (12).

In summary, the long wavelength q_{\parallel} dispersion of the q_{\perp} dependent plasmons including the optical and the

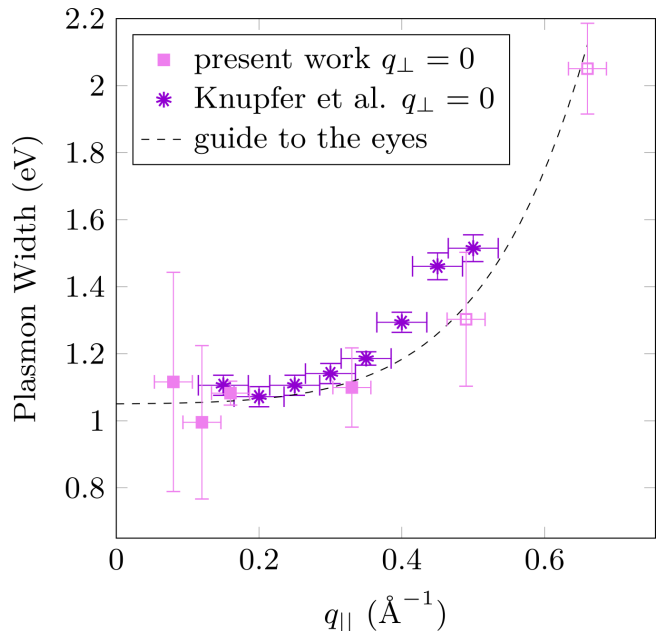


FIG. 5. Plasmon width at half maximum in dependence on the momentum transfer parallel to the layers at $q_{\perp} = 0$. For comparison the corresponding data from a Drude fit of our previous EELS measurements reported in Ref. [36] was added as dark purple stars. The excitations in the continuum range are marked by open symbols.

acoustic collective excitations and the decay of the optical plasmon by Landau damping can be all explained in terms of a mean-field RPA model. It is possible to understand this interpretation of the present results in the following way. Long wavelength charge excitations are not influenced by local interactions such as on-site Coulomb and Hund's exchange interactions. This behaviour is different from ARPES studies, in which local properties play an important role. In this context it is also important to note that monopole (a single hole) excitations detected in ARPES are differently screened compared to dipole excitations recorded in EELS. We further emphasize that our present analysis of the acoustic plasmon dispersion is also important for the understanding of previous [29, 30, 44] and future RIXS studies on cuprates.

VI. PERSPECTIVES

The present study has demonstrated that optical and acoustic plasmons can be investigated by T-EELS in the complete BZ in layered systems. Therefore, with the advent of higher energy resolution, T-EELS will be competitive at lower energies with RIXS, also taking into account that momentum-resolved T-EELS provides a direct probe of the dynamic susceptibility. It will be possible to study in more detail the different influence of correlation effects on optical and acoustic plasmons, caused

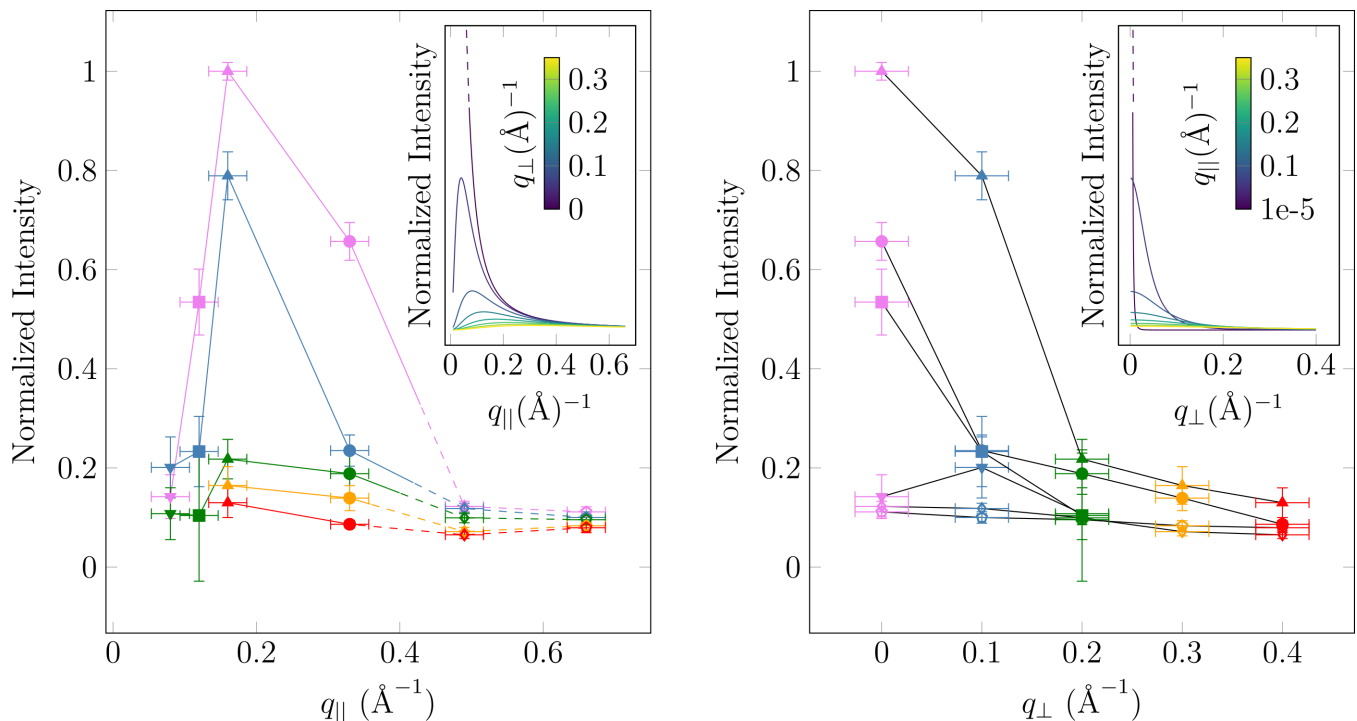


FIG. 6. Integrated loss intensities under the fitted plasmon peaks as a function of in-plane (q_{\parallel}) and out-of-plane (q_{\perp}) momentum transfer. The q_{\perp} values 0, 0.1, 0.2, 0.3, and 0.4 \AA^{-1} are marked by purple, blue, green, yellow, and red colour symbols, respectively (see Fig. 3). The q_{\parallel} values 0.08, 0.12, 0.16, 0.33, 0.49, and 0.66 \AA^{-1} are marked by tip down triangles, squares, tip up triangles, circles, diamonds, and pentagons, respectively. The dashed lines and open symbols indicate the single particle continuum regime. The insets show the dependency predicted by the coupled 2D plasmon model due to Ref. [38]. At $q_{\perp} = q_{\parallel} = 0$ the curves diverge indicated by a dashed line.

by an energy dependent effective mass. The latter was predicted by a combined density functional/ dynamical mean-field theory (DFT + DMFT) calculation [51] and experimentally detected by optical spectroscopy [46]. Furthermore, in "strange" metals, it will be possible to study low-energy and high-momentum charge excitations which were predicted in Ref. [52] to depend on correlation effects. In this way it will be possible to evaluate the spatial dependence of the density-density fluctuations in "strange" metals.

VII. METHODS

A. Dielectric Response of the Layered Plasmon System

The dielectric function corresponding to the Fetter model of a system of coupled 2D layers reads [38]

$$\epsilon(\omega, q_{\parallel}, q_{\perp}) = 1 - \frac{2\pi N e^2 q_{\parallel} / m}{\omega(\omega + i\Gamma) - s^2 q_{\parallel}^2} \frac{\sinh(q_{\parallel} d)}{\cosh(q_{\parallel} d) - \cos(q_{\perp} d)}. \quad (13)$$

This dielectric function is an approximation assuming a perturbation charge that is confined to the 2D layers supporting the plasmons, which is violated by the electron

beam resulting in deviations to the experimental dielectric response. However, the intensities of the plasmon peaks can be derived from this dielectric function by calculating the loss probability (T-EELS signal) using Eq. 1 and integration along ω (see Fig. 6).

A version of the long wave wavelength sum rule for the dynamic susceptibility reads [50]

$$\lim_{q \rightarrow 0} \Im \left(\frac{1}{\epsilon(q, \omega)} \right) = -\frac{\pi \omega_{\text{P}}}{2} (\delta(\omega - \omega_{\text{P}}) - \delta(\omega + \omega_{\text{P}})). \quad (14)$$

Thus, in the $q \rightarrow 0$ limit, the dynamic susceptibility is determined by the longitudinal plasmon.

B. Samples

Sr_2RuO_4 crystals were grown using the floating-zone method [53]. The superconducting transition temperature of the sample was $T_c = 1.5 \text{ K}$.

Thin TEM lamellas of Sr_2RuO_4 with the normal pointing along \mathbf{b} were prepared by Focused Ion Beam (FIB) using a Thermofisher instrument. The target thickness of the lamellas was 80 nanometers. Low ion energy polishing was used as final step to thin Ga-ion damaged surface layers.

C. EELS measurements

The momentum-resolved loss function was recorded at a FEI Titan³ TEM equipped with a Wien monochromator and a Gatan Tridiem imaging filter (GIF) at 80 kV acceleration voltage in a serial way (i.e., one EEL spectrum per fixed momentum). The energy resolution is around 120 meV (FWHM of zero loss peak). Using a camera length (i.e., effective distance between sample and detector) of 1.15 m. The GIF entrance aperture was used to select the different momentum values and covers a momentum range of 0.04 \AA^{-1} (0.13 mrad semi collection angle). The acquisition times are presented in Table 1.

TAB. I. Acquisition times (in sec) for the used momentum transfers (in \AA^{-1}).

q_{\perp} \backslash q_{\parallel}	0.08	0.12	0.16	0.33	0.49	0.66
0	2	5	5	5	10	10
0.1	5	5	5	5	10	10
0.2	5	5	5	5	10	10
0.3	10	10	10	10	10	10
0.4	10	10	10	10	10	10

Due to instabilities of the monochromator and the rather long collection times required at large momentum transfers, the recorded spectra are subject to substantial noise as well as mutual random fluctuations/offsets. In order to mitigate these effects, each spectrum was separately aligned with the help of the quasi-elastic peak. After alignment of the zero loss position a superposition of the following three functions was fitted to the spectra. i) an asymmetric Pseudo-Voigt-profile ($V = c \left(\eta \frac{1}{1+(\omega-\omega_0)^2/(\lambda(\omega)\sigma)^2} + (1-\eta) \exp \left[-\ln(2) \left(\frac{\omega-\omega_0}{\sigma} \right)^2 \right] \right)$)

with $\lambda(\omega) = 1|_{\omega \leq 0}$ and $\lambda(\omega) > 1|_{\omega > 0}$ reflecting the quasi elastic peak including ultra-low-loss excitations such as phonons, ii) a Drude-like function $I(\omega) = a \frac{\omega_p^2 \omega \Gamma}{(\omega^2 - \omega_p^2)^2 + (\omega \Gamma)^2}$ corresponding to the plasmon peaks and iii) a phenomenological background following a linear function. Finally, the spectral positions and half widths of the plasmons were derived from the fitted parameters ω_p and Γ of the Drude function. The intensity (Fig. 6) corresponds to the area under the fitted Drude peak, which is obtained by integrating the latter over ω .

D. Fermi velocities and susceptibility

For the calculation of the Fermi velocity along the [100] direction and the bare particle susceptibility $\chi_0(q_{\parallel}, 0, \omega)$ we used a TB band structure [47] based on a LDA band structure. We use a multi-band version of Eq. 2 and taking only intra-band excitations with the same matrix element into account, thus neglecting inter-band excitations which may be caused by a strong spin-orbit coupling, which leads to a k-dependence of the orbital character of the bands [49]. Mainly the β and the γ bands contribute to $\langle v_F^2 \rangle_{100}$ and χ_0 .

VIII. DATA AVAILABILITY

All data supporting the findings are provided as figures in the article. Data files for all figures are available at <https://opara.zih.tu-dresden.de//handle/123456789/763> and from the corresponding authors on request.

IX. REFERENCES

-
- [1] J. Zaanen, Planckian dissipation, minimal viscosity and the transport in cuprate strange metals, *SciPost Phys.* **6**, 061 (2019).
 - [2] R. A. Cooper, Y. Wang, B. Vignolle, O. J. Lipscombe, S. M. Hayden, Y. Tanabe, T. Adachi, Y. Koike, M. Nohara, H. Takagi, C. Proust, and N. E. Hussey, Anomalous Criticality in the Electrical Resistivity of $\text{La}_{2-x}\text{Sr}_x\text{CuO}_4$, *Sci.* **323**, 603 (2009).
 - [3] T. Valla, A. V. Fedorov, P. D. Johnson, B. O. Wells, S. L. Hulbert, Q. Li, G. D. Gu, and N. Koshizuka, Evidence for Quantum Critical Behavior in the Optimally Doped Cuprate $\text{Bi}_2\text{Sr}_2\text{CaCu}_2\text{O}_{8+\delta}$, *Sci.* **285**, 2110 (1999).
 - [4] K. T. N. E. Hussey and H. Takagi, Universality of the Mott-Ioffe-Regel limit in metals, *Philos. Mag.* **84**, 2847 (2004).
 - [5] C. M. Varma, P. B. Littlewood, S. Schmitt-Rink, E. Abrahams, and A. E. Ruckenstein, Phenomenology of the normal state of Cu-O high-temperature superconductors, *Phys. Rev. Lett.* **63**, 1996 (1989).
 - [6] M. R. Norman and C. Pépin, The electronic nature of high temperature cuprate superconductors, *Rep. Prog. Phys.* **66**, 1547 (2003).
 - [7] J. Lindhard, *Kgl. Danske Videnskab. Selskab, Mat.-phys. Medd* **28**, 8 (1954).
 - [8] H. Raether, *Excitation of plasmons and interband transitions by electrons* (Springer Verlag, Berlin, 1980).
 - [9] S. Schnatterly, *Inelastic Electron Scattering Spectroscopy* (Academic Press, 1979) pp. 275–358.
 - [10] J. Fink, *Recent Developments in Energy-Loss Spectroscopy* (Academic Press, 1989) pp. 121–232.
 - [11] N. Nücker, H. Romberg, S. Nakai, B. Scheerer, J. Fink, Y. F. Yan, and Z. X. Zhao, Plasmons and interband transitions in $\text{Bi}_2\text{Sr}_2\text{CaCu}_2\text{O}_8$, *Phys. Rev. B* **39**, 12379 (1989).
 - [12] Y.-Y. Wang, G. Feng, and A. L. Ritter, Electron-energy-loss and optical-transmittance investigation of

- Bi₂Sr₂CaCu₂O₈, Phys. Rev. B **42**, 420 (1990).
- [13] H. Romberg, N. Nuecker, J. Fink, T. Wolf, X. X. Xi, B. Koch, H. Geserich, M. Dürller, W. Assmus, and B. Gegenheimer, Dielectric function of YBa₂Cu₃O_{7-δ} between 50 meV and 50 eV, Z. Phys. B Cond. Matter **78**, 367 (1990).
- [14] N. Nücker, U. Eckern, J. Fink, and P. Müller, Long-wavelength collective excitations of charge carriers in high-*T_c* superconductors, Phys. Rev. B **44**, 7155 (1991).
- [15] M. Knupfer, G. Roth, J. Fink, J. Karpinski, and E. Kaldis, Plasmon dispersion and the dielectric function in YBa₂Cu₄O₈ single crystals, Phys. C: Supercond. **230**, 121 (1994).
- [16] F. Roth, A. Revcolevschi, B. Büchner, M. Knupfer, and J. Fink, Evidence for an orbital dependent Mott transition in the ladders of (La, Ca)_xSr_{14-x}Cu₂₄O₄₁ derived by electron energy loss spectroscopy, Phys. Rev. B **101**, 195132 (2020).
- [17] M. Terauchi, M. Tanaka, T. Takahashi, H. Katayama-Yoshida, T. Mochiku, and K. Kadowaki, Electron-Energy-Loss Spectroscopy of Oxide Superconductor Bi₂Sr₂CaCu₂O₈, Jpn. J. Appl. Phys. **34**, L1524 (1995).
- [18] TERAUCHI, TANAKA, TSUNO, and ISHIDA, Development of a high energy resolution electron energy-loss spectroscopy microscope, J. Microsc. **194**, 203 (1999).
- [19] A. Romero-Bermúdez, A. Krikun, K. Schalm, and J. Zaanen, Anomalous attenuation of plasmons in strange metals and holography, Phys. Rev. B **99**, 235149 (2019).
- [20] S. T. Van den Eede, T. J. N. van Stralen, C. F. J. Flipse, and H. T. C. Stoof, Plasmons in a layered strange metal using the gauge-gravity duality, Phys. Rev. B **109**, 085119 (2024).
- [21] M. Mitrano, A. A. Husain, S. Vig, A. Kogar, M. S. Rak, S. I. Rubeck, J. Schmalian, B. Uchoa, J. Schneeloch, R. Zhong, G. D. Gu, and P. Abbamonte, Anomalous density fluctuations in a strange metal, Proc. Natl. Acad. Sci. USA **115**, 5392 (2018).
- [22] A. A. Husain, M. Mitrano, M. S. Rak, S. Rubeck, B. Uchoa, K. March, C. Dwyer, J. Schneeloch, R. Zhong, G. D. Gu, and P. Abbamonte, Crossover of charge fluctuations across the strange metal phase diagram, Phys. Rev. X **9**, 041062 (2019).
- [23] A. A. Husain, E. W. Huang, M. Mitrano, M. S. Rak, S. I. Rubeck, X. Guo, H. Yang, C. Sow, Y. Maeno, B. Uchoa, T. C. Chiang, P. E. Batson, P. W. Phillips, and P. Abbamonte, Pines' demon observed as a 3D acoustic plasmon in Sr₂RuO₄, Nature 10.1038/s41586-023-06318-8 (2023).
- [24] J. Chen, X. Guo, C. Boyd, S. Bettler, C. Kengle, D. Chaudhuri, F. Hoveyda, A. Husain, J. Schneeloch, G. Gu, P. Phillips, B. Uchoa, T.-C. Chiang, and P. Abbamonte, Consistency between reflection momentum-resolved electron energy loss spectroscopy and optical spectroscopy measurements of the long-wavelength density response of Bi₂Sr₂CaCu₂O_{8+x}, Phys. Rev. B **109**, 045108 (2024).
- [25] E. Mauri, S. Smit, M. S. Golden, and H. T. C. Stoof, Gauge-gravity duality comes to the laboratory: Evidence of momentum-dependent scaling exponents in the nodal electron self-energy of cuprate strange metals, Phys. Rev. B **109**, 155140 (2024).
- [26] V. G. Grigoryan, G. Paasch, and S.-L. Drechsler, Determination of an effective one-electron spectrum from the plasmon dispersion of nearly optimally doped Bi₂Sr₂CaCu₂O₈, Phys. Rev. B **60**, 1340 (1999).
- [27] A. vom Felde, J. Sprösser-Prou, and J. Fink, Valence-electron excitations in the alkali metals, Phys. Rev. B **40**, 10181 (1989).
- [28] A. Fleszar, R. Stumpf, and A. G. Eguiluz, One-electron excitations, correlation effects, and the plasmon in cesium metal, Phys. Rev. B **55**, 2068 (1997).
- [29] M. Hepting, L. Chaix, E. W. Huang, R. Fumagalli, Y. Y. Peng, B. Moritz, K. Kummer, N. B. Brookes, W. C. Lee, M. Hashimoto, T. Sarkar, J.-F. He, C. R. Rotundu, Y. S. Lee, R. L. Greene, L. Braicovich, G. Ghiringhelli, Z. X. Shen, T. P. Devereaux, and W. S. Lee, Three-dimensional collective charge excitations in electron-doped copper oxide superconductors, Nature **563**, 374 (2018).
- [30] A. Nag, M. Zhu, M. Bejas, J. Li, H. C. Robarts, H. Yamase, A. N. Petsch, D. Song, H. Eisaki, A. C. Walters, M. García-Fernández, A. Greco, S. M. Hayden, and K.-J. Zhou, Detection of acoustic plasmons in hole-doped lanthanum and bismuth cuprate superconductors using resonant inelastic X-Ray scattering, Phys. Rev. Lett. **125**, 257002 (2020).
- [31] A. Singh, H. Y. Huang, C. Lane, J. H. Li, J. Okamoto, S. Komiyama, R. S. Markiewicz, A. Bansil, T. K. Lee, A. Fujimori, C. T. Chen, and D. J. Huang, Acoustic plasmons and conducting carriers in hole-doped cuprate superconductors, Phys. Rev. B **105**, 235105 (2022).
- [32] Y. Maeno, H. Hashimoto, K. Yoshida, S. Nishizaki, T. Fujita, J. G. Bednorz, and F. Lichtenberg, Superconductivity in a layered perovskite without copper, Nature **372**, 532 (1994).
- [33] C. Bergemann, A. P. Mackenzie, S. R. Julian, D. Forsythe, and E. Ohmichi, Quasi-two-dimensional Fermi liquid properties of the unconventional superconductor Sr₂RuO₄, Adv. Phys. **52**, 639 (2003).
- [34] A. P. Mackenzie, R. K. W. Haselwimmer, A. W. Tyler, G. G. Lonzarich, Y. Mori, S. Nishizaki, and Y. Maeno, Extremely Strong Dependence of Superconductivity on Disorder in Sr₂RuO₄, Phys. Rev. Lett. **80**, 161 (1998).
- [35] L. de' Medici, J. Mravlje, and A. Georges, Janus-faced influence of Hund's rule coupling in strongly correlated materials, Phys. Rev. Lett. **107**, 256401 (2011).
- [36] M. Knupfer, F. Jerzembeck, N. Kikugawa, F. Roth, and J. Fink, Propagating charge carrier plasmons in Sr₂RuO₄, Phys. Rev. B **106**, L241103 (2022).
- [37] D. Grecu, Plasma frequency of the electron gas in layered structures, Phys. Rev. B **8**, 1958 (1973).
- [38] A. L. Fetter, Electrodynamics of a layered electron gas. II. Periodic array, Ann. Phys. **88**, 1 (1974).
- [39] S. Das Sarma and J. J. Quinn, Collective excitations in semiconductor superlattices, Phys. Rev. B **25**, 7603 (1982).
- [40] A. Greco, H. Yamase, and M. Bejas, Plasmon excitations in layered high-*T_c* cuprates, Phys. Rev. B **94**, 075139 (2016).
- [41] P. Abbamonte and J. Fink, Collective charge excitations studied by electron energy-loss spectroscopy, arXiv:2404.04670 (2024).
- [42] P. M. Platzman and P. A. Wolff, *Waves and interactions in solid state plasmas* (Academic Press, New York, 1973).
- [43] H. Ehrenreich and M. H. Cohen, Self-consistent field approach to the many-electron problem, Phys. Rev. **115**, 786 (1959).
- [44] M. Hepting, M. Bejas, A. Nag, H. Yamase, N. Coppola, D. Betto, C. Falter, M. Garcia-Fernandez, S. Agrestini, K.-J. Zhou, M. Minola, C. Sacco, L. Maritato, P. Or-

- giani, H. I. Wei, K. M. Shen, D. G. Schlom, A. Galdi, A. Greco, and B. Keimer, Gapped collective charge excitations and interlayer hopping in cuprate superconductors, *Phys. Rev. Lett.* **129**, 047001 (2022).
- [45] M. Apostol, Plasma frequency of the electron gas in layered structures, *Z. Phys. B Condens. Matter* **22**, 13 (1975).
- [46] D. Stricker, J. Mravlje, C. Berthod, R. Fittipaldi, A. Vecchione, A. Georges, and D. van der Marel, Optical Response of Sr_2RuO_4 Reveals Universal Fermi-Liquid Scaling and Quasiparticles Beyond Landau Theory, *Phys. Rev. Lett.* **113**, 087404 (2014).
- [47] A. Liebsch and A. Lichtenstein, Photoemission Quasiparticle Spectra of Sr_2RuO_4 , *Phys. Rev. Lett.* **84**, 1591 (2000).
- [48] P. Batson and J. Silcox, Experimental energy-loss function, $\text{Im}[-1/\varepsilon(q, \omega)]$, for aluminum, *Phys. Rev. B* **27**, 5224 (1983).
- [49] A. Tamai, M. Zingl, E. Rozbicki, E. Cappelli, S. Riccò, A. de la Torre, S. McKeown Walker, F. Y. Bruno, P. D. C. King, W. Meevasana, M. Shi, M. Radović, N. C. Plumb, A. S. Gibbs, A. P. Mackenzie, C. Berthod, H. U. R. Strand, M. Kim, A. Georges, and F. Baumberger, High-Resolution Photoemission on Sr_2RuO_4 Reveals Correlation-Enhanced Effective Spin-Orbit Coupling and Dominantly Local Self-Energies, *Phys. Rev. X* **9**, 021048 (2019).
- [50] G. D. Mahan, *Many-Particle Physics, Third Edition* (Plenum, New York, 2000).
- [51] X. Deng, J. Mravlje, R. Žitko, M. Ferrero, G. Kotliar, and A. Georges, How bad metals turn good: Spectroscopic signatures of resilient quasiparticles, *Phys. Rev. Lett.* **110**, 086401 (2013).
- [52] G. Khaliullin and P. Horsch, Theory of the density fluctuation spectrum of strongly correlated electrons, *Phys. Rev. B* **54**, R9600 (1996).
- [53] J. S. Bobowski, N. Kikugawa, T. Miyoshi, H. Suwa, H. shu Xu, S. Yonezawa, D. A. Sokolov, A. P. Mackenzie, and Y. Maeno, Improved Single-Crystal Growth of Sr_2RuO_4 , *Condens. Matter* **4**, 6 (2019).

ACKNOWLEDGMENTS

J.F. thanks P. Abbamonte, R. von Baltz, S.-L. Drechsler, and A. Greco for helpful discussions. This work is supported by a KAKENHI Grants-in-Aids for Scientific Research (Grants No. 18K04715, No. 21H01033, and No. 22K19093), and Core-to-Core Program (No. JPJSCCA20170002) from the Japan Society for the Promotion of Science (JSPS) and by a JST-Mirai Program (Grant No. JPMJMI18A3). J.S. received funding from the HORIZON EUROPE framework program for research and innovation under grant agreement n. 101094299. A.L. and M.K. acknowledge funding from the Deutsche Forschungsgemeinschaft (DFG, German Research Foundation)-project-id 461150024. B.B. received funding from the Würzburg-Dresden Cluster of Excellence on Complexity and Topology in Quantum Matter – ct.qmat (EXC 2147, project-id 390858490).

X. AUTHOR CONTRIBUTIONS

J.F., M.K., A.L., and B.B. conceived the experiment, J.S. and D.W. performed the EELS experiment. J.S. and J.F. analyzed the data. F.J. and N.K. prepared and characterized the samples. J.F. calculated the susceptibility. J.F., J.S. and A.L. wrote the manuscript with input from all authors.